# On the Structure of the Velocity Field over Progressive Mechanically-Generated Water Waves

YIANNIS ALEX. PAPADIMITRAKIS,[1] EN YUN HSU, AND ROBERT L. STREET

*Environmental Fluid Mechanics Laboratory, Department of Civil Engineering, Stanford University, Stanford, CA 94305*

(Manuscript received 10 June 1983, in final form 21 September 1984)

ABSTRACT

The structure of the velocity field over a propagating wave of fixed frequency is examined. The vertical and horizontal velocities were measured in a transformed Eulerian wave-following frame of reference in a wind-wave research facility at Stanford University. Experimental results are given for seven different wind speeds in the range 140–402 cm $s^{-1}$, with 1 Hz, 2.54 cm nominal amplitude, mechanically-generated sinusoidal water waves.

The mean velocity profiles have a log–linear form with a wake free-stream characteristic. The constant $C$ which characterizes these profiles decreases with increasing wind speed, as a result of the variation of surface roughness condition between the transition region and the fully rough regime. The wave-associated stresses with their main component at twice the fundamental wave frequency were found to be significant. Therefore, the nonlinear terms encountered in the wave-induced Navier-Stokes equations associated with these stresses cannot be neglected, and linearization of the above equations is not permissible. The wave-induced velocity field and the wave-perturbed turbulence were found to depend significantly on the ratio of the wave speed to the mean free-stream wind velocity, $c/U_{\delta_0}$.

## 1. Introduction

In two previous papers, Papadimitrakis *et al.* (1983, 1984) reported simultaneous measurements of the fluctuating pressure and velocity fields in the air boundary layer above progressive, mechanically-generated water waves in order to evaluate their contribution to the momentum and energy transfer processes and study the effects of the mobile and deformable boundary on the Reynolds-stress production mechanism. This study describes in detail the structure of the mean, wave-induced, and turbulent velocity fields in the air.

The knowledge of the detailed structure of these fields is valuable for understanding a variety of different problems such as: 1) the generation and growth of water waves; 2) the gas and heat exchange processes at the air–water interface; and 3) the transport of pollutants in the atmospheric boundary layer and water enclosures. Although several experimental and theoretical investigations of both the pressure and velocity fields in the air boundary layer exist, their results show considerable disagreement. For wave generation studies, because the most important manifestation of this phenomenon in the air occurs at small heights above the instantaneous water surface, it is necessary that the measuring instruments be as nearly flush with the air–water interface as possible. For this reason, the velocity field was measured with an "X" hot film mounted on a wave-following device operating in a transformed coordinate system similar to that used by Hsu *et al.* (1981) and Hsu and Hsu (1983). These Eulerian wave-following measurements were taken at preselected distances from the instantaneous water surface.

## 2. Experimental apparatus—data acquisition and analysis

### a. Experiment

The experiments were conducted in the Stanford wind-wave research tunnel (Hsu, 1965), modified by the authors to facilitate measurements of the fluctuating pressure in the air boundary layer (Papadimitrakis, 1982). It has a test section 20 m long, beginning at the air-flow inlet. The data-acquisition station was located 13 m from the inlet. The depth of the air flow $H$ ($=2\delta_0$) was measured from the mean water level to the channel roof. The water depth $d$ was 0.83 m and $H$ = 1.07 m. The generated 1 Hz, sinusoidal wave was in deep water, with a wave length $L$ = 1.56 m and a wave number $k$ = 4.03 $m^{-1}$. To ensure a smooth air flow into the channel and to increase the boundary layer thickness, a 1.52 m long flat plate with an array of phenolic spires at the upper end was installed at the air inlet (Ligrani *et al.*, 1979).

[1] Present affiliation: College of Marine Studies, University of Delaware, Lewes Complex, Lewes, DE 19958.

The air flow above the progressive, small-amplitude (i.e., wave slope $\leq 0.1$), water waves is considered to be two-dimensional. In the Cartesian coordinate system used in this investigaton $x$ is measured in the wave propagation or mean air-flow direction, and $y$ is the vertical coordinate, measured upward from the mean water level (MWL). The coordinate transformation used contains only vertical translation, namely,

$$t = t^*, \quad x = x^*, \quad y = y^* + f(y^*)\tilde{\eta}, \quad (2.1a,b,c)$$

$$f(y^*) = \frac{\sinh(kH - ky^*)}{\sinh(kH)}, \quad (2.2)$$

and has been described in detail by Hsu *et al.* (1981); $\tilde{\eta}$ represents the sinusoidal component of the water surface displacement from the MWL. Since $f(0) = 1$ and $f(H) = 0$, it follows that $y^* = 0$ corresponds to the air–water interface and $y = y^* = H$ corresponds to the roof of the laboratory wind-wave facility. Apparently $y^*$ = constant represents a streamline of potential flow over the wave without wind.

To measure the flow in the transformed wave-following frame, the wave-follower system developed by Yu *et al.* (1971), modified by Hsu *et al.* (1981), and modified again by the authors was used as the primary instrument. The system allows one to set both the mean elevation $y^*$ (with respect to the instantaneous water surface) within $\pm 0.25$ mm and the oscillation amplitude $a_{wf}$ according to the calibration relationship:

$$a_{wf} = \frac{\sinh(kH - ky^*)}{\sinh(kH)} a, \quad (2.3)$$

using the signal output of a fixed wave-height gage as input. Here $a$ represents the amplitude of the sinusoidal water wave as measured by the wave-height gage. The details of operating the wave-follower system in a manner of decreasing the amplitude of oscillations with height, according to (2.1c, 2.2) and the reasoning behind the coordinate transformation have also been reported by Hsu *et al.* (1981). The wave-follower system and probe arrangement can be found in Papadimitrakis (1982) and Hsu *et al.* (1981).

Wave-height gauges were used to obtain the water-wave characteristics and drive the wave-follower; they were of capacitance type (Colonell, 1966) with an accuracy in static and dynamic calibration tests of $\pm 0.25$ mm. A pitot-static tube was used as a reference to calibrate the hot-films used to measure the velocity field in the air (Hsu *et al.*, 1981). These films were TSI Model 1248-10 end-flow "X" probes, 0.0254 mm in diameter, 0.508 mm long, and 0.51 mm apart, with a flat frequency response up to 40 000 Hz; they were operated in a constant-temperature mode. The films were calibrated *in situ* (i.e., in the core region of the wind tunnel) immediately prior to data recording. The uncertainty in the hot-film calibration for the mean velocity was 3%. However, for the measured turbulent quantities such as turbulent Reynolds stresses, the uncertainty is higher and was estimated to be approximately 8%.

### b. Data acquisition–reduction

The hot-film signals were zero-suppressed, amplified, and low-pass filtered at 250 Hz to fulfill the Nyquist criterion, as samples were taken every 0.002 s, for 184.32 s. The phase shifts introduced by the low-pass filters were found to be negligible in the range 1–6 Hz, where the wave-induced velocity components are expected to be significant; 180 blocks of 7680 digitized data points (including pressure, wave-height, and wave-follower potentiometer data) were recorded at each measurement point on tape for later analysis, using the computer system described by Takeuchi and Mogel (1975). The air and water flows were permitted to settle into a statistical equilibrium over a half-hour period prior to data acquisition. Occasionally, the water was preheated for several hours in order to reach the air temperature and thus create isothermal conditions across the air boundary layer. The data taken correspond to seven different mean free-stream velocities in the range 140–402 cm $s^{-1}$, with 1 Hz, 2.54 cm nominal amplitude, mechanically-generated sinusoidal water waves; they were collected at 20 or 21 elevations ranging from 0.75 to 53.3 cm above the interface.

Since the instantaneous velocity field above the waves consists of a mean, a wave-induced perturbation and a turbulent component, viz.,

$$u_i = U_i + \tilde{u}_i + u_i', \quad i = 1, 2; \quad (2.4)$$

familiar time and phase averages were used to extract the wave-induced fluctuations from the total velocity signals. The phase average contains only the mean and wave-induced parts, and therefore

$$\tilde{u}_i = \langle u_i \rangle - U_i, \quad (2.5)$$

where $U_i$ is the time-averaged mean velocity, $\tilde{u}_i$ the wave-induced perturbation, $u_i'$ the turbulent fluctuation, and angle brackets denote phase averaging. The vertical wave-induced velocity was corrected to account for the spurious component introduced by the wave-follower motion. Cross- and autospectral analyses for $\tilde{u}_i$ using $\tilde{\eta}$ as a reference were performed by fast-Fourier transformation (FFT) to determine the amplitude and phase of each harmonic contained in $\tilde{u}_i$ (Hsu *et al.*, 1981). These quantities were also determined by curve fitting the recorded data with a cosine waveform of frequency $\omega$ and/or its harmonics (Papadimitrakis, 1982). The latter technique was also used to cross-check some of the wave-induced velocity results with oscillatory behavior obtained through phase averaging and cross-spectral analysis.

## 3. Results

### a. General

In this section the physical quantities measured in the air, such as velocities and Reynolds stresses, are presented together with a discussion of their features. Comparisons with other studies are also made when appropriate. Time-averaged mean, wave-induced, and phase-averaged quantities are used to describe the velocity field. These quantities, normalized with the channel centerline mean velocity $U_{\delta_0}$ and/or $U_{\delta_0}^2$, are generally presented in nondimensional profile distributions as a function of $y^*/\delta_0$ ordinate. The wave-induced quantity $\tilde{u}_i$, denoted by

$$\tilde{u}_i = |\hat{u}_i| \cos(\omega t + \theta_{\tilde{u}_i}) + \text{harmonics}, \qquad (3.1)$$

contains the fundamental mode and all the harmonics. The harmonics of both the $\tilde{u}$ and $\tilde{v}$ velocity components were found through spectra analysis to be weak (less than 10% of the fundamental), in agreement with Hsu *et al.* (1981). Hence the wave-perturbation quantities can be approximated by their fundamental mode without changing the overall conclusions.

### b. Water surface roughness

The ripples riding the mechanically-generated water waves are small but visible. Their rms values representing the mean roughness of the water surface on the mechanically-generated waves are shown in Table 1. The total mean water roughness including the generated wave can also be found from the wave-height records. Therefore, the surface condition depending on the roughness height $y_0$, and characterized by the roughness parameter $\mathrm{Re}^* = y_0 u_*/\nu$, where

$$y_0 = (\overline{\eta'^2})^{1/2} \quad \text{or} \quad (\overline{\tilde{\eta}^2})^{1/2} \quad \text{and} \qquad \overline{\tilde{\eta}^2} \approx 0.5a^2 + \overline{\eta'^2} \qquad (3.2a,b)$$

may vary from aerodynamically smooth to fully rough according to traditional measures; $u_*$, $\nu$ are the friction velocity and the kinematic viscosity of the air, respectively. The total mean roughness and the roughness parameter for both cases are also shown in Table 1.

### c. Time-averaged mean velocity field

The time-averaged mean velocity field (hereafter called mean) is presented in terms of mean velocity and mean turbulent stress profiles. These quantities characterize the mean turbulent flow upon which the wave perturbated velocities and Reynolds stresses are imposed.

#### 1) Mean velocity profiles

Figure 1 shows the mean wind profiles in semi-log coordinates ($U$ versus $\ln y^*$). The lower part represents the logarithmic region of a typical turbulent-boundary-layer velocity profile, while the upper part shows the wake characteristic. For higher wind speeds the wake becomes more pronounced, the elevation where it begins to be felt lower, and the lower portion of the profile close to the water surface deviates from the logarithmic distribution. There the velocity magnitudes are larger than those predicted by the log law. This deviation may be attributed to generation of the surface drift current whose magnitude is proportional to the wind speed (Wu, 1975), provided $y^* = 0$ corresponds to the air–water interface according to Eqs. (2.1c) and (2.2). The wake characteristic of the mean velocity profiles was also observed by Young *et al.* (1973), Chen (1981), Hsu *et al.* (1981) and Hsu and Hsu (1983) in the Stanford wind wave research facility.

The experimental data for the mean velocities were curve-fitted, in a least-squares sense, to the wake log–linear expression:

$$\frac{U_{\delta_0} - U_i}{u_*} = -\frac{1}{\kappa}\ln\left(\frac{y_i^*}{\delta}\right) + \frac{\pi(x)}{\kappa}\left[1 + \cos\left(\frac{\pi y_i^*}{\delta}\right)\right], \qquad (3.3)$$

proposed by Coles (1968) to determine $u_*$, $\delta$ and

TABLE 1. Water-wave roughness.

| | $U_{\delta_0}$ (cm s$^{-1}$) | | | | | | |
|---|---|---|---|---|---|---|---|
| | 141 | 179 | 200 | 231 | 285 | 346 | 402 |
| $y_{01} = (\eta'^2)^{1/2}$ (mm) | 0.25 | 0.50 | 0.50 | 0.25 | 0.75 | 1.25 | 1.50 |
| $y_{02} = (\tilde{\eta}^2)^{1/2}$ (mm) | 19.50 | 20.00 | 18.25 | 19.25 | 18.25 | 18.50 | 19.25 |
| $\mathrm{Re}_1^* = \frac{y_{01}u_*}{\nu}$ | 0.70 | 1.60 | 1.50 | 1.40 | 3.90 | 9.40 | 14.30 |
| $\mathrm{Re}_2^* = \frac{y_{02}u_*}{\nu}$ | 53 | 70 | 72 | 90 | 99 | 140 | 192 |

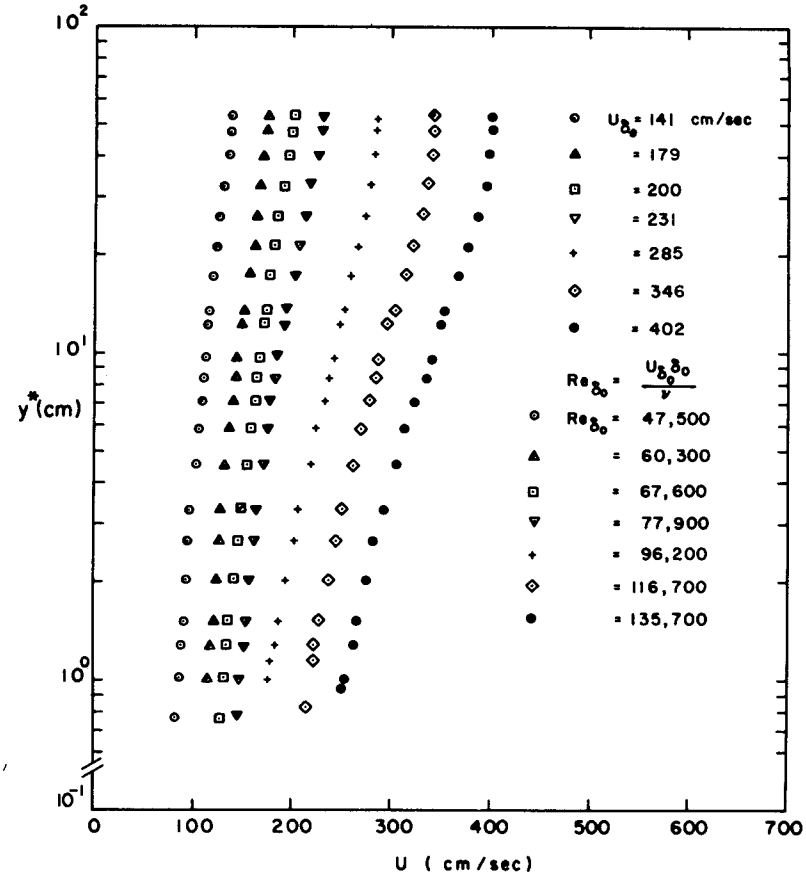


FIG. 1. Mean velocity profiles.

$\pi(x)$; $\kappa$, $\delta$ are the Von Karman constant and the boundary layer thickness, respectively. In wall coordinates the above expression yields

$$u^+ = \frac{1}{\kappa}\ln y^+ + C + \frac{\pi(x)}{\kappa}\left[1 - \cos\left(\frac{\pi y^+}{\delta^+}\right)\right], \quad (3.4)$$

where

$$u^+ = \frac{U}{u_*}; \quad y^+ = \frac{y^* u_*}{\nu}; \quad \delta^+ = \frac{\delta u_*}{\nu};$$

$$C = u^+_{\delta_0} - \frac{1}{\kappa}\ln\delta^+ - 2\frac{\pi(x)}{\kappa}. \quad (3.5a,b,c,d)$$

Table 2 lists the determined parameters $u_*$, $\pi(x)$, $C$, $\delta^+$, and the values of the friction velocities $u_*$ calculated from the measured shear stress in the constant stress layer region. The wake log-linear expression proposed by Finley to correct the discrepancy of Eq. (3.3), which yields $\partial U/\partial y^* = u_*/\kappa\delta_0 \neq 0$ at the channel centerline, were also used to fit our mean velocity data. Both methods gave, within 10%, similar results for $u_*$ and $\pi(x)$, provided each of them is quite sensitive to the extent of the fitting region.

The values of $\pi(x)$ shown in Table 2, with the exception of run 5, where $U_{\delta_0}$ = 285 cm s$^{-1}$, agree well with the observation that $\pi = \pi(\beta)$ for equilibrium layers, where $\beta = (\delta_1/\tau_0)(dP/dx)$ represents the ratio of pressure to shear forces, $\delta_1$, $\tau_w$, and $P$ represent the displacement thickness, surface shear stress and mean static pressure, respectively. These values agree with the empirical expression given by Mellor and Gibson (1966), viz.,

$$\pi(x) \approx 0.8(\beta + 0.5)^{0.75} \quad (3.6)$$

since $dP/dx$ and therefore $\beta$ is negative in our facility. The measured value of 0.53 corresponding to the lowest wind speed $U_{\delta_0}$ = 141 cm s$^{-1}$, where $|dP/dx|$ is small, agrees well with the value $\pi(x)$ = 0.55 proposed by Coles (1968) for zero pressure gradient flows. At $U_{\delta_0}$ = 285 cm s$^{-1}$, both schemes gave $\pi(x) \approx -0.15$, which seems to be unrealistic, provided negative $\pi(x)$ implies a decrease in the mean velocities as one approaches the free-stream. No simple explanation could be found for this peculiar behavior. The decreasing values of $\pi(x)$ at higher wind speeds are the result of deeper penetration of the region of

TABLE 2. Mean velocity profile characteristics.

| $U_{\delta_0}/c$ (cm s$^{-1}$) | $u_*$ (cm s$^{-1}$) | $\pi(x)$ | $C$ | $\delta^+$ | $(-\overline{u'v'})^{1/2}$ |
|---|---|---|---|---|---|
| 141 | 4.3 | 0.53 | 12.8 | 1453 | 2.7 |
| 179 | 5.5 | 0.34 | 12.4 | 1886 | 3.5 |
| 200 | 6.2 | 0.30 | 11.9 | 1922 | 4.4 |
| 231 | 7.2 | 0.43 | 10.8 | 2425 | 5.1 |
| 346 | 11.9 | 0.31 | 7.5 | 2725 | 10.4 |
| 402 | 15.6 | 0.26 | 4.1 | 3556 | 12.5 |

intermittency into the boundary layer as $dP/dx$ becomes large and negative, or quoting Coles (1968), ". . . because of the more pronounced corner effect."

The values of $u_*$ obtained by the profile technique are seen to be larger than the turbulence data. The equivalence of turbulent Reynolds stress, however, to $u_*^2$ is valid only in the inertial subrange (Tennekes and Lumley, 1972, p. 156). This behavior was also observed by Takeuchi *et al.* (1977) and Chen (1981) under similar wind conditions. Velocity spectral measurements of the latter showed that the flow has practically no inertial subrange and therefore equivalence of the friction velocity to the turbulent Reynolds stress may not be valid. According to Tennekes and Lumley (1972),

$$-\frac{\overline{u'v'}}{u_*^2} \approx 1 - \frac{1}{\kappa y^+}; \quad \text{therefore}$$

$$u_*^2 \approx -\frac{\overline{u'v'}}{1 - 1/\kappa y^+}. \qquad (3.7a,b)$$

Since $\kappa y^+ > 1$ for our lowest point of measurements and the constant stress layer region, it follows that $u_*^2 > -\overline{u'v'}$. Furthermore, the turbulent Reynolds number defined as $\mathrm{Re}_\lambda = \sigma_u \lambda/\nu$, where $\lambda$ is the Taylor microscale and $\sigma_u = (\overline{u'^2})^{1/2}$, is expected to be small ($\sim$10) for low wind speeds, and therefore the condition $\mathrm{Re}_\lambda^{3/4} \gg 1$ (Hinze, 1975, p. 228) for the existence of inertial subrange may not be satisfied there. This behavior is shown in our data where the agreement between $u_*$ and $(-\overline{u'v'})^{1/2}$ becomes better at the higher wind speeds. Although some data in the Stanford wind-wave facility (Young *et al.*, 1973; McIntosh *et al.*, 1975, etc.) show a frequency band with a slope of $-5/3$ in the $u'$ velocity spectra, this is not a true indication of the existence of an inertial subrange, since their $v'$ spectra do not attain the required ratio of 4/3 to the $u'$ spectra in this frequency band.

The value of $C$ shown in Table 2 is not an absolute constant, but decreases as the wind speed increases. This result implies that the mechanically-generated water wave is part of the surface roughness, as Stewart (1967) suggested. The decreasing values of $C$ for higher wind speeds suggest that it has the form:

$$C = C_0 - \frac{\Delta U}{u_*}, \qquad (3.8)$$

where $C_0$ is an absolute constant and the velocity decrement $\Delta U/u_*$ is a function of the surface roughness condition. The small variation of $C$ in the range of wind speeds 140–200 cm s$^{-1}$ agrees well with the behavior of the roughness function $B$ of a typical rough flat-plate boundary layer, as shown in Fig. 20.21 in Schlichting (1968, p. 583). The value $C$ is expected to be greater than its fixed-surface counterpart for the low wind speed range, because of the relative surface stress decrease due to the development of the drift current. For the high wind speed studies (say, $U_{\delta_0}/c > 2.2$), ripples become prominent surface roughness on the water waves, and the shear stress increase caused by them is greater than the corresponding relative stress reduction produced by the drift current. Thus, for low and moderate wind speeds the friction velocity $u_*$ and the constant $C$ are smaller and greater, respectively, over water waves than their corresponding values over a rigid surface, but the opposite is true for high wind speeds. This behavior was also observed by Chen (1981), who found that for high wind speeds $u_*$ was greater than its counterpart value over a rigid wavy surface. Since the roughness Reynolds number $\mathrm{Re}_2^*$ shown in Table 2 falls between the transition and the fully rough regimes according to the flat-plate boundary layer classification, we may conclude that the measured values of $C$ are consistent with the description of Eq. (3.8). Most of the investigators mentioned earlier in this section observed this rough surface behavior of mean velocity profiles. However, their corresponding values for $C$ are different because they didn't include the wake effect of the outer region of the boundary layer.

A typical velocity profile in wall coordinates is shown in Fig. 2. The artificially increased boundary layer thickness ranging approximately from 49 to 36

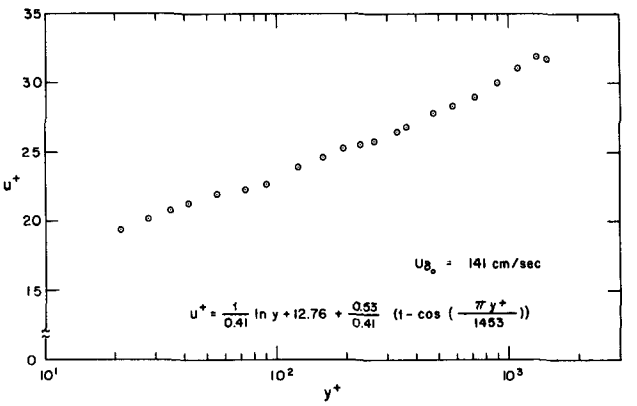


FIG. 2. Typical mean horizontal velocity profile in wall coordinates.

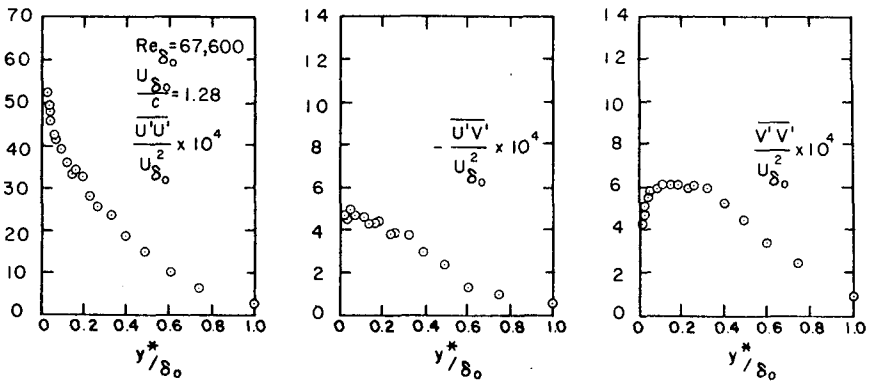


FIG. 3. Mean turbulent Reynolds stress distribution.

cm was found to be considerably greater than that reported by previous investigators, and for the low wind speed studies it was extended almost up to the channel centerline. This result, combined with the fact that the air flow produced by the transition plate had statistical properties representative of natural boundary layers (at least up to the level of the turbulent correlations),[2] clearly suggests that the transition plate largely accomplished its purpose as an artificial boundary layer thickening device.

#### 2) MEAN TURBULENT REYNOLDS STRESSES

Typical mean turbulent Reynolds stress profiles are shown in Figs. 3. The magnitudes of $\overline{u'u'}$ are approximately one order larger than those of $-\overline{u'v'}$ and $\overline{v'v'}$. This order of magnitude difference is also observed in other types of turbulent wall-bounded shear flows. An almost constant stress layer near the wave surface is observed in each profile of $-\overline{u'v'}$. The decrease of shear stress at the lowest portion of the constant stress layer can be attributed to the damping of turbulence by viscosity. The non-normalized mean turbulent Reynolds stresses tend to increase with wind speed. Because the flow considered in this study is a turbulent shear flow of boundary layer type, turbulence is more active near the interface, decreasing rapidly towards the centerline region of the channel. These features are also shown in Figs. 3. They were observed by Chen (1981) and also by Hsu *et al.* (1981) and Hsu and Hsu (1983).

### *d. Wave-induced velocity fields*

#### 1) GENERAL

The wave-perturbation velocity field consists of the wave-induced velocities $\tilde{u}_i$, the wave-associated Reynolds stresses $\tilde{u}_i\tilde{u}_j$, and the wave-induced turbulent Reynolds stresses $\tilde{r}_{ij}$, defined as: $\tilde{r}_{ij} = \langle u_i'u_j' \rangle - \overline{u_i'u_j'}$.

#### 2) WAVE-INDUCED VELOCITIES

The phase-averaged results for $\tilde{u}$ and $\tilde{v}$ were used to deduce the amplitudes $|\hat{u}|$ and $|\hat{v}|$ and the phase lags $\theta_{\tilde{u}}$ and $\theta_{\tilde{v}}$ through spectra analysis. Figures 4 and 5 show representative amplitude (±5%) and phase (±5°, ±3°) distributions of the wave-induced velocities $\tilde{u}$ and $\tilde{v}$. Near the wave surface the magnitudes of $\tilde{u}$ and $\tilde{v}$ are strongly related to the ratio $U_{\delta_0}/c$. For $U_{\delta_0}/c < 1$, $|\hat{u}|$ decreases as $U_{\delta_0}/c$ increases, while for $U_{\delta_0}/c \geqslant 1$, $|\hat{u}|$ increases with $U_{\delta_0}/c$, with one exception at $U_{\delta_0}/c = 1.28$. The magnitude of $|\hat{v}|$ decreases with increasing $U_{\delta_0}/c$. Both $|\hat{u}|$ and $|\hat{v}|$ profiles display an exponential decay behavior. At the free stream the magnitudes of $|\hat{u}|$ and $|\hat{v}|$ are almost equal, but near the interface their ratio depends on whether $U_{\delta_0}/c \lesssim 1$.

The surface boundary conditions for $\tilde{u}$ and $\tilde{v}$ yield $\theta_{\tilde{u}} = 0°$ and $\theta_{\tilde{v}} = 270°$. The measured phase $\theta_{\tilde{v}}$ approaches 270° as $y^*/\delta_0 \to 0$ except for the higher wind speeds. Because the boundary condition for $\tilde{u}$ at the interface was deduced from inviscid analysis and viscosity plays an important role there, it is expected that $\theta_{\tilde{u}}$ cannot be zero as $y^*/\delta_0 \to 0$, at least for the low and moderate wind speeds. As $U_{\delta_0}/c$ becomes large, the water surface behaves as a rigid wave (for $c \to 0$, $U_{\delta_0}/c \to \infty$), with a boundary condition $\theta_{\tilde{v}} = 0$ at $y^* = 0$. Both the trend in the observed values of $\theta_{\tilde{v}}$ at the lowest point of measurements and the data of Chen (1981) over a rigid wavy surface support this argument. In most cases the phase difference between $\tilde{u}$ and $\tilde{v}$ in the free stream is close to 90°, providing strong evidence for the inviscid potential character of the wave-perturbed flow there. Further evidence of this potential character can be found in the distributions of the mean wave-associated shear stress. The small magnitude of this stress suggests that the mean flow and the wave-perturbation field are almost decoupled in the free stream. On the other hand, a close to 180° phase

[2] As the comparison with results without the transition plate shows (Chen, 1981; Hsu *et al.*, 1981; and Hsu and Hsu, 1983).

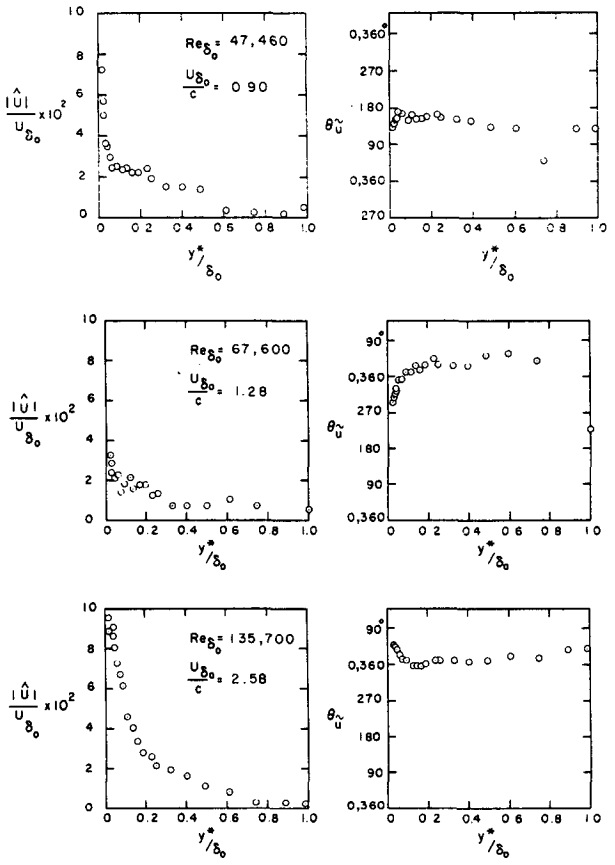


FIG. 4. Horizontal wave-induced velocity amplitude and phase distribution.

shift between $\theta_{\tilde{u}}$ and $\theta_{\tilde{v}}$ near the interface shows the strong coupling between the mean flow and the wave-perturbation field. This coupling in the boundary layer results in different magnitudes of $|\hat{u}|$ and $|\hat{v}|$ and in the phase shifts of $\theta_{\tilde{u}}$ and $\theta_{\tilde{v}}$ shown in Figs. 4 and 5.

A careful inspection of the wave-induced velocity field at $U_{\delta_0}/c = 1.28$ reveals some interesting features of the flow at this particular wind speed. Since the critical height is located at $y_c^* \approx 5$ cm, it is obvious that the parts of the air flow below and above $ky_c^* \approx 0.2$ are exposed to different mechanisms, as Hsu and Hsu (1983) have pointed out. The amplitude $|\hat{u}|$ as a function of wind speed has its smallest value near the interface, and its distribution throughout the boundary layer has a somewhat irregular exponential behavior. The phase $\theta_{\tilde{u}}$ approaches 270° in the water proximity, while for all other wind speeds it varies between 0 and 180°. The amplitude $|\hat{v}|$ has a local minimum there before it begins to increase again at about $U_{\delta_0}/c = 1.83$. The phase $\theta_{\tilde{v}}$ decreases to 90° close to the edge of the boundary layer and remains constant from there on, in contrast to its almost uniform distribution for the other wind speeds. The stresses $\overline{\tilde{u}\tilde{u}}$ and $\overline{\tilde{v}\tilde{v}}$ also have their smallest values, but they show a more regular exponential behavior. The peculiar structure of the velocity field at this particular wind speed was also observed by Chen (1981) at $U_{\delta_0}/c = 1.21$ and is probably related to the location of the recirculating zones (cat's eyes) observed in a frame moving with the wave and to the undulations of the critical layer, which is very thick, highly nonlinear, and turbulently diffusive, as Hsu and Hsu (1983) have shown.

Aside from the above peculiarities, the overall behavor of $\tilde{u}$ and $\tilde{v}$ agrees well with that observed by Hsu *et al.* (1981) and Hsu and Hsu (1983), with small differences in the detailed distributions of both the amplitude and phase shifts in the outer and free stream regions. However, our Reynolds number based on $\delta_0$ for a particular $U_{\delta_0}/c$, is slightly greater than that of Chen (1981), Hsu *et al.* (1981) and Hsu and Hsu (1983) because of the larger $\delta_0$ used in this study. An additional explanation for the differences found may be provided by the higher uncertainty of these quantities away from the interface, due to their small magnitudes there.

The strong influence of $U_{\delta_0}/c$ on the behavior of both $\tilde{u}$ and $\tilde{v}$ may be attributed to the viscous

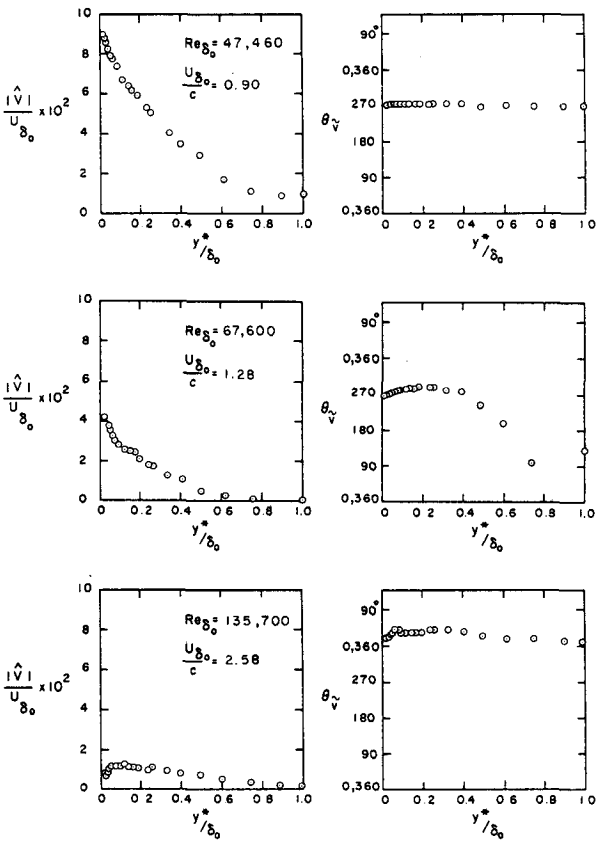


FIG. 5. Vertical wave-induced velocity amplitude and phase distribution.

character of Stokes layer near the interface, whose thickness is $=(2\nu/\omega)^{1/2} = 0.22$ cm (Phillips, 1977, p. 46) and to the concentrated vorticity in the neighborhood of the critical layer. When $U_{\delta_0}/c < 1$, there is no critical layer in the air flow, and viscosity in the Stokes layer dominates the wave-perturbation behavior. For $U_{\delta_0}/c \geq 1$, the highly concentrated vorticity in the critical layer alters the wave-perturbation structure.

### 3) Mean wave-associated Reynolds stresses

Figures 6 show typical distributions of the mean wave-associated Reynolds stresses $\tilde{u}_i\tilde{u}_j$ (±10%) as a function of $U_{\delta_0}/c$ or the corresponding Reynolds number $\mathrm{Re}_{\delta_0}$. The wave-associated Reynolds stresses are important in transferring energy from the mean flow to the wave-perturbation field. This energy is ultimately transmitted by the wave-induced pressure across the interface and causes the wave's growth. The rate of energy transfer per unit volume from the mean flow to the wave-perturbation field is given by $-\tilde{u}\tilde{v}(\partial U/\partial y^*)$. Because $\partial U/\partial y^* > 0$ inside the boundary layer, it follows that the direction of energy transfer depends on the sign of $-\tilde{u}\tilde{v}$. As Figs. 6 show, the sign of this stress changes throughout the boundary layer, in agreement with Chen, Hsu *et al.*, and Hsu and Hsu, except for $U_{\delta_0}/c = 2.22$ and 2.58, where surprisingly enough $\tilde{u}\tilde{v}$ remains positive. This picture suggests that the energy drains either from the mean field to the waves or vice versa, depending on $U_{\delta_0}/c$ and the specific location within the boundary layer.

### 4) Phase-averaged wave-associated stresses

The main component (fundamental mode) of the phase-averaged wave-associated stress $\langle \tilde{u}_i\tilde{u}_j \rangle$ appears at twice the fundamental water wave frequency, as it can readily be seen from the relationship:

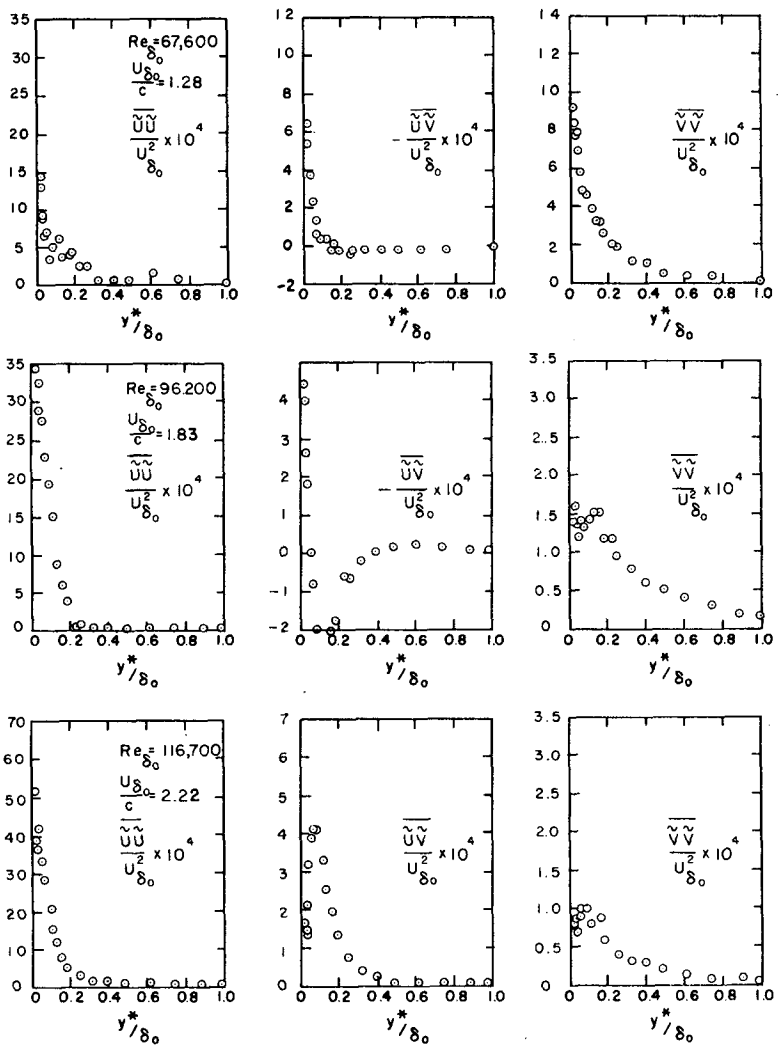


FIG. 6. Mean wave-associated stress distribution.

$$\langle \tilde{u}_i\tilde{u}_j \rangle = |\hat{u}_i||\hat{u}_j| \cos(\omega t^* - kx^* - \theta_{\tilde{u}_i}) \times \cos(\omega t^* - kx^* - \theta_{\tilde{u}_j})$$

$$= \frac{1}{2}|\hat{u}_i||\hat{u}_j|[\cos(2\omega t^* - 2kx^* - \theta_{\tilde{u}_i} - \theta_{\tilde{u}_j}) + \cos(\theta_{\tilde{u}_i} - \theta_{\tilde{u}_j})]. \quad (3.8)$$

Therefore, the harmonics of $\langle \tilde{u}_i\tilde{u}_j \rangle$ stresses appear at frequencies 4, 6, 8 Hz, etc., for 1 Hz mechanically-generated water wave. This behavior is apparently shown in Figs. 7, representing typical phase averaged $\langle \tilde{u}\tilde{v} \rangle$ stress distributions for the various wind speeds considered in this study.

The distribution of the ratio $\overline{\tilde{u}\tilde{v}}/\overline{u'v'}$ as either a function of the wind speed or $y^*/\delta_0$ is shown in Figs. 8 and 9. A positive dimensionless value indicates a downward flux of momentum from this term. Kendall (1970) and, with some exceptions, Takeuchi *et al.* (1977) found the wave-associated stress to be positive and negative below and above the critical height. This contradicts the results of Lai and Shemdin (1971), who found large negative contributions to the $u$, $v$ cospectra (a downward flux) at the wave frequency when $c/U_{\delta_0} < 1$. Our data support Takeuchi *et al.* (1977) measurements and, with some exceptions, those of Kendall (1970).

### 5) WAVE-INDUCED REYNOLDS STRESSES

The wave-induced turbulent stresses represent the coupling between the wave-induced field and the background turbulence and transmit energy directly to the waves. Figures 10, 11 and 12 show typical amplitude (±8%) and phase (±10°) distributions of these stresses. The phase-averaged results were used to calculate the amplitude and phase $|\hat{r}_{ij}|$, $\theta_{\hat{r}_{ij}}$ through spectral analysis. The amplitudes $|\hat{r}_{ij}|$ are large near the interface and decrease as $y^*/\delta_0$ increases. This decrease, however, is not monotonic, but shows an oscillatory behavior. A dip is occasionally observed in the $|\hat{r}_{ij}|$ profiles, with a corresponding phase jump, but no consistent pattern can be discerned. The oscillatory behavior of the $|\hat{r}_{ij}|$ amplitudes was also found by Gent and Taylor (1976) in calculations of the interface flow in a curvilinear coordinate system under finite-amplitude wave conditions. A consistent increase of the peak value of $|\hat{r}_{ij}|$ with increasing wind speed can also be seen in the same figures. The decrease in $|\hat{r}_{ij}|$ as $y^*/\delta_0 \to 0$ is again due to the viscosity damping.

With the exception of the free-stream, where the phase distributions usually become erratic due to the small stress magnitudes, it can be seen that both $\tilde{r}_{11}$ and $\tilde{r}_{22}$ have similar phase distributions, while $\tilde{r}_{12}$ has approximately a 90° constant phase difference with

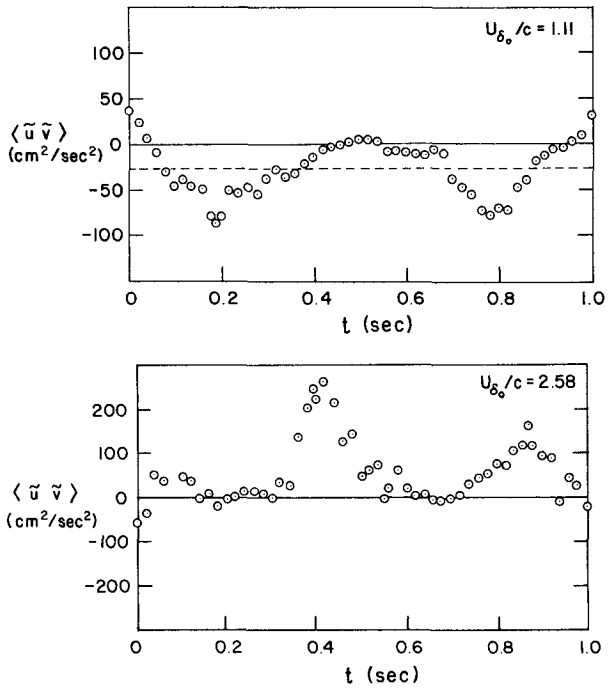


FIG. 7. $\tilde{u}\tilde{v}$ phase-averaged distribution.

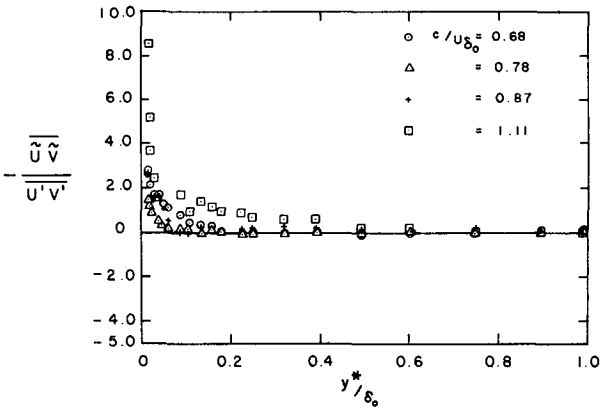


FIG. 8. Distribution of the ratio $\overline{\tilde{u}\tilde{v}}/\overline{u'v'}$.

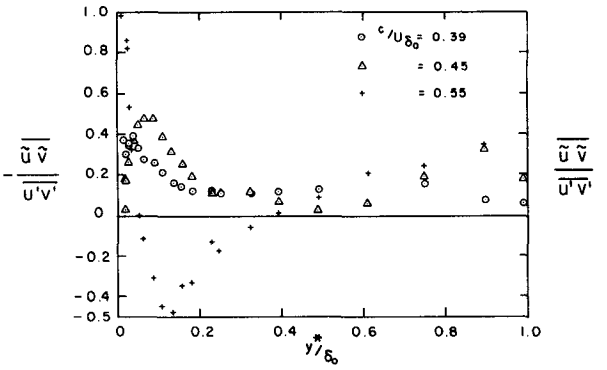


FIG. 9. As in Fig. 8 but for $c/U_{\delta_0}$ = 0.39 to 0.55. Note that + reads on the right side of the graph.

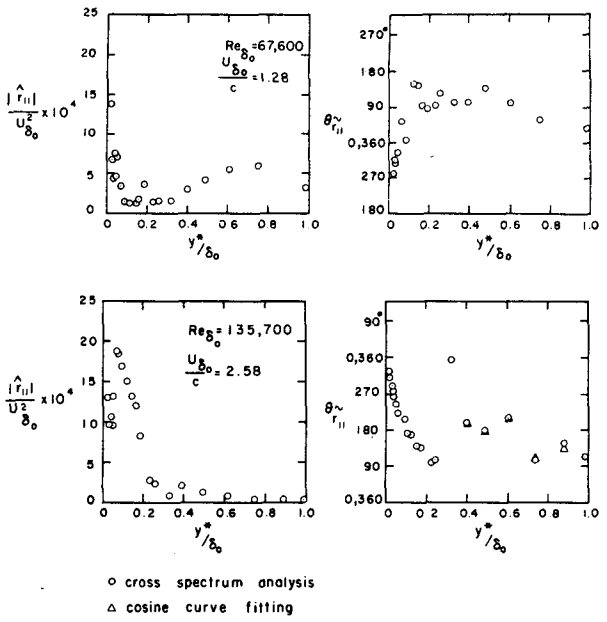


FIG. 10. Amplitude and phase distribution of $\tilde{r}_{11}$.

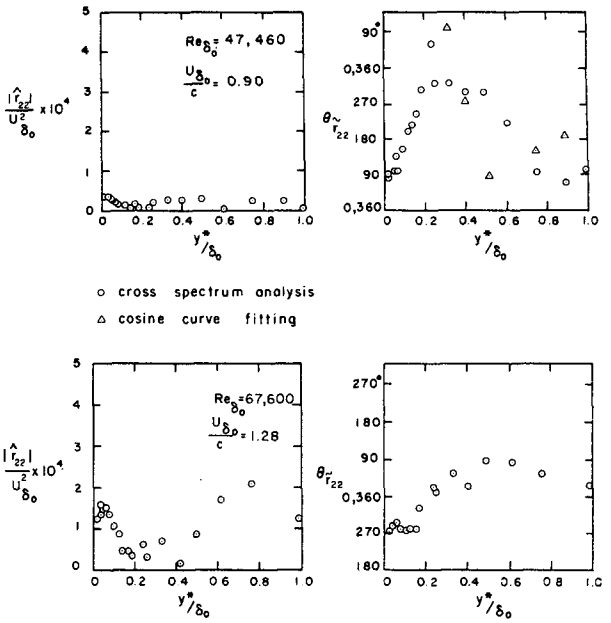


FIG. 12. As in Fig. 10 but of $\tilde{r}_{22}$.

respect to $\tilde{r}_{11}$ and $\tilde{r}_{22}$ throughout the boundary layer. Phase lags computed by the cosine curve-fitting technique, for those cases which show erratic free-stream phase distribution, are also included in the corresponding figures. Because $\langle \tilde{u}_i \tilde{u}_j \rangle$ appears mainly at 2 Hz, no contamination of the $\tilde{r}_{ij}$ behavior by the wave-associated stresses is expected. A more consistent pattern in the phase distributions is obtained, for some wind speeds, but the improvement cannot be considered dramatic. At $U_{\delta_0}/c = 1.28$ the amplitudes $|\tilde{r}_{11}|$ and $|\tilde{r}_{12}|$ again show a distinct behavior. For $ky^* \geq 0.8$, they become considerably larger than their counterpart values at any other wind speed. The small magnitude of these and the wave-associated stresses and their peculiar characteristics at this wind speed manifest themselves in the behavior of the measured wave-induced pressure (Papadimitrakis, 1982), which was also found to fluctuate in both the amplitude and phase throughout the boundary layer.

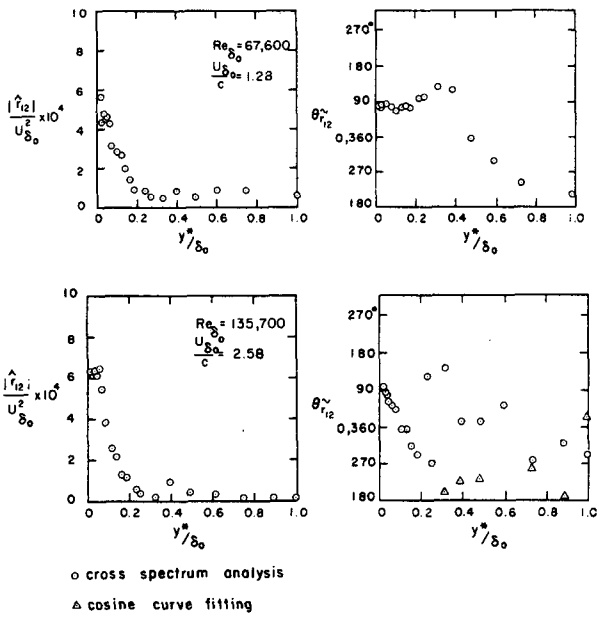


FIG. 11. As in Fig. 10 but of $\tilde{r}_{12}$.

Chen (1981) showed that, in the channel centerline region, $\tilde{r}_{11}$ and $\tilde{r}_{22}$ should be in phase and $\tilde{r}_{12}$ 180° out of phase with $\tilde{u}$ while, near the water surface, $\tilde{r}_{11}$ and $\tilde{r}_{12}$ should be roughly in phase with $\tilde{\eta}$. Our results confirm these special features of $\theta_{\tilde{r}_{ij}}$, within the uncertainty limits. The 180° phase jump observed by Hsu *et al.* (1981) in their $\theta_{\tilde{r}_{ij}}$ profiles does not seem to be a universal feature of interface flows. This finding agrees well with Chen and later measurements of Hsu and Hsu. Although the amplitude dip does not always reach zero as it should (provided there is a phase jump of 180°), because of probable misalignment between the oscillatory probe positions and the locations where the flow has a constant value of $\langle u_i' u_j' \rangle$, its presence implies that the $\tilde{r}_{ij}$ stress is exerted in opposite directions just above and below the point in discussion, and therefore the phase jump appears as a necessity to (i) bring the values of $\theta_{\tilde{r}_{11}}$ and $\theta_{\tilde{r}_{12}}$ in the water proximity back to approximately 0 and 90° whenever they are close to 180 and 90° and (ii) guarantee that the maximum turbulence intensity and shear stress occurs at the appropriate side of the wave crest, depending on whether $U_{\delta_0}/c \gtrless 1$, as

discussed in the following paragraph. The above phase values are considered only approximate, since to some extent $\tilde{r}_{ij}$ also depends on the wave-induced velocities. In general the observed wave-induced stress amplitude and phase behavior agree well with those described by Chen and Hsu and Hsu, given that the corresponding $\mathrm{Re}_{\delta_0}$ for the same wind speed is somewhat different.

Typical phase-averaged results for $u'v'$ at the lowest point of measurements, shown also in Figs. 13, demonstrate that this stress is relatively high on the windward side of the water wave, with the exception of lowest wind speed run, where $U_{\delta_0}/c < 1$. This behavior is consistent with the measurements of Okuda *et al.* (1977), Toba (1978), Okuda (1982), Hsu *et al.* (1981) and the prediction of Gent and Taylor (1976) and can be attributed to the response of turbulence to a varying mean flow. It is well known that the turbulence intensity increases in a decelerating mean flow; therefore the air flow in a frame of reference moving with the waves is regarded as the flow over a series of convergent and divergent regions undergoing acceleration and deceleration. When $U_{\delta_0}/c < 1$ the mean flow is in the minus $x$ direction and acceleration occurs at the lee side of the crest. Consequently, the turbulence intensity and the shear stress become maximum there. The opposite is true when $U_{\delta_0}/c > 1$. For high enough wind speeds, significant contributions to $\langle u'v' \rangle$ are also observed on the leeward side of the wave crests. These figures also show that the $\langle u'v' \rangle$ stress contains other harmonics whose magnitudes are small compared to that of the fundamental mode as a result of the nonlinear wave–turbulence interactions.

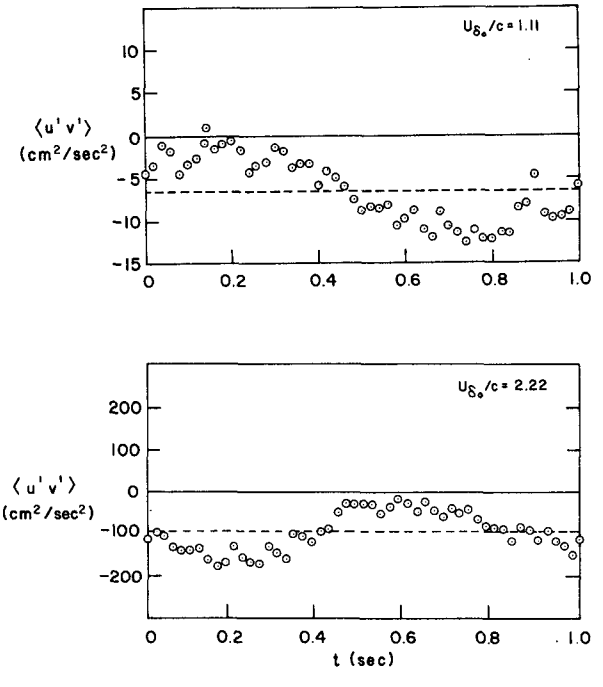


FIG. 13. $\langle u'v' \rangle$ phase-averaged distribution.

## 4. Summary and conclusions

The results and discussions presented in the previous section suggest the following conclusions:

1) The water surface condition, based on the total mean wave roughness, varies between the transition region and the fully rough regime. As a result, the constant $C$ in the mean velocity profile expression decreases with increasing wind speed. At low wind speeds $C$ is greater than its corresponding value over fixed surfaces, due to the relative reduction of surface stress caused by the drift current. At high wind speeds the opposite is true, because the surface-stress increase due to the greater roughness produced by the water ripples exceeds the corresponding stress reduction produced by the wind drift. Therefore, the friction velocity $u_*$ becomes smaller and/or greater than its counterpart value over a fixed surface, depending on the local wind speed.

2) The log–linear form of mean velocity profiles, their wake free-stream characteristic, and the similarity between the mean turbulent Reynolds stress profiles and those observed over a flat surface clearly indicate that the transformed coordinate system given by Eqs. (2.1a,b,c) provides the best description of interface flows with mechanically-generated water waves.

3) The wave-associated stresses have their main component at 2 Hz for a 1 Hz, mechanically-generated sinusoidal water wave, and their harmonics appear at 4, 6 Hz, etc. Therefore the terms

$$\frac{\partial}{\partial x_j}(\tilde{u}_i\tilde{u}_j - \overline{\tilde{u}_i\tilde{u}_j})$$

usually discarded in the linear analysis of the wave-induced Navier-Stokes equations, cannot be neglected, and linearization of these equations is not permissible. These and the wave-induced Reynolds stresses, with their main component at the fundamental water wave frequency, are partially responsible for the strong wave-induced pressure harmonics measured by the authors (Papadimitrakis, 1982).

4) The data presented show that waves influence the air flow above them. Both the wave-induced and turbulent velocity-field characteristics depend on $c/U_{\delta_0}$. The wave-associated Reynolds stress $-\overline{\tilde{u}\tilde{v}}$ tends to be negative for high wind speeds and positive for low.

*Acknowledgments.* This work was supported by the National Science Foundation through Grant NSF-CEE-7817618. The authors are thankful to the referees for their valuable comments and suggestions.

## REFERENCES


Chen, F., 1981: Experimental approach to closure modeling of turbulent shear flow over a wavy surface, Ph.D. dissertation, Civil Eng. Dept., Stanford University, 219 pp.

Coles, D. E., 1968: The Young Person's Guide to the Data, *Computation of Turbulent Boundary Layer: 1968 AFOSR-IFP-Stanford Conference,* Vol. II, 1–45.

Colonell, J. M., 1966: Laboratory simulation of sea waves, Civil Eng. Dept., Tech. Rep. No. 65, Stanford University.

Gent, P. R., and P. A. Taylor, 1976: A Numerical Model of the Air Flow above Water Waves, *J. Fluid Mech.,* **77,** 105-ff.

Hinze, J. O., 1975: *Turbulence—An Introduction to Its Mechanism and Theory,* McGraw-Hill, 790 pp.

Hsu, E. Y., 1965: A wind, water-wave research facility. Civil Engrg. Dept., Tech. Rep. No. 57, Stanford University.

Hsu, C. T., E. Y. Hsu and R. L. Street, 1981: On the structure of turbulent flow over a progressive water wave: Theory and experiments in a transformed wave-following coordinate system. Part 1, *J. Fluid Mech.,* **105,** 87–117.

——, and ——, 1983: On the structure of turbulent flow over a progressive water wave: Theory and experiment in a transformed wave-following coordinate system. Part 2, *J. Fluid Mech.,* **131,** 123–153.

Kendall, J. J., Jr., 1970: The turbulent boundary layer over a wall with progressive surface waves, *J. Fluid Mech.,* **41,** 259–281.

Lai, R. J., and O. H. Shemdin, 1971: "Laboratory investigation of air turbulence above simple water waves," *J. Geoph. Res.,* **76,** 7334–7350.

Ligrani, P. M., W. M. Kays and R. J. Moffat, 1979: The thermal and hydrodynamic behavior of thick, rough-wall, turbulent boundary layers, Mech. Eng. Dept., Tech. Rep. No. HMT-29, Stanford University.

McIntosh, D. A., R. L. Street and E. Y. Hsu, 1975: Turbulent heat and momentum transfer at an air–water interface: The influence of surface conditions, Civil Eng. Dept., Tech. Rep. No. 197, Stanford University.

Mellor, G. L., and D. M. Gibson, 1966: Equilibrium turbulent boundary layers, *J. Fluid Mech.,* **24,** 225–253.

Okuda, K., S. Kawai and Y. Toba, 1977: Measurements of skin friction flow along the surface of wind waves," *J. Oceanogr. Soc. Japan,* **33,** 190-ff.

——, 1982: Internal flow structure of short wind waves. Part II. The streamline pattern," *J. Oceanogr. Soc. Japan,* **38,** 313–322.

Papadimitrakis, Y. A., 1982: Velocity and pressure measurements in the turbulent boundary layer above mechanically-generated water waves," Ph.D. dissertation, Civil Eng. Dept., Stanford University, 445 pp.

——, E. Y. Hsu and R. L. Street, 1983: Measurements of the fluctuating pressure in the turbulent boundary layer over progressive, mechanically-generated water waves, *Gas Transfer at Water Surfaces,* W. Brutsoert and G. H. Jirka, Eds., Reidel.

——, —— and ——, 1984: The structure of the turbulent boundary layer over a mobile and deformable boundary, *Ninth Biennial Symp. on Turbulence,* University of Missouri-Rolla.

Phillips, O. M., 1977: *The Dynamics of the Upper Ocean.* Cambridge University Press, 336 pp.

Schlichting, H., 1968: *Boundary Layer Theory.* McGraw-Hill, 748 pp.

Stewart, R. W., 1967: Mechanics of the air–sea interface, *Phys. Fluids,* **10** (Suppl), pp. S47–55.

Takeuchi, K., and T. R. Mogel, 1975: A performance evaluation of a mini-computer, *Rev. Sci. Instrum.,* **46,** 691.

Takeuchi, K., E. Leavitt and S. P. Chao, 1977: Effects of water waves on the structure of turbulent shear flow, *J. Fluid Mech.,* **80,** 535–559.

Tennekes, H., and J. L. Lumley, 1972: *A First Course in Turbulence,* MIT Press, 300 pp.

Toba, Y., 1979: Study on wind waves as a strongly nonlinear phenomenon, *Proc. 12th Symp. Naval Hydrodynamics,* National Academy of Sciences, Washington, D.C.

Wu, J., 1975: Wind-induced drift currents, *J. Fluid Mech.,* **68,** 49–70.

Young, M. B. O., E. Y. Hsu and R. L. Street, 1973: Air-water interaction: the nature of turbulent heat, mass, and momentum transfer mechanisms in the air boundary layer, Civil Eng. Dept., Tech. Rep. No. 163, Stanford University.

Yu, H. Y., E. Y. Hsu and R. L. Street, 1971: A refined measurement of aerodynamic pressure over progressive water waves, Civil Eng. Dept., Rep. No. 146, Stanford University.